



PAPER

Ultrasonic guided wave-based switch rail monitoring using independent component analysis

To cite this article: Jianjun Wu *et al* 2018 *Meas. Sci. Technol.* **29** 115102

View the [article online](#) for updates and enhancements.

You may also like

- [Diffusion geometry approach to efficiently remove electrical stimulation artifacts in intracranial electroencephalography](#)

Sankaraleengam Alagapan, Hae Won Shin, Flavio Fröhlich et al.

- [Automated EEG artifact elimination by applying machine learning algorithms to ICA-based features](#)

Thea Radünz, Jon Scouter, Olaf Hochmuth et al.

- [Performance limits of ICA-based heart rate identification techniques in imaging photoplethysmography](#)

Kavan Mannapperuma, Benjamin D Holton, Peter J Lesniewski et al.

The advertisement features a dark blue background with white and orange text. On the left, there's a smartphone icon displaying the book cover of 'The Breath Biopsy® Guide Fourth edition'. A large white circle with the word 'FREE' in blue is overlaid on the phone icon. To the right of the phone, the title 'The Breath Biopsy® Guide' is written in large white font, with 'Fourth edition' in blue below it. A decorative pattern of white molecular structures is in the top right. At the bottom, a blue button says 'DOWNLOAD THE FREE E-BOOK' in white. To the right of the button is an orange square with the 'BREATH BIOPSY' logo. To the far right is the 'OWLSTONE MEDICAL' logo.

Ultrasonic guided wave-based switch rail monitoring using independent component analysis

Jianjun Wu¹, Zhifeng Tang², Fuzai Lv¹, Keji Yang¹, Chung Bang Yun³ and Yuanfeng Duan³

¹ State Key Laboratory of Fluid Power and Mechatronic Systems, Zhejiang University, Hang Zhou, People's Republic of China

² Institute of Advanced Digital Technologies and Instrumentation, Zhejiang University, Hang Zhou, People's Republic of China

³ College of Civil Engineering and Architecture, Zhejiang University, Hang Zhou, People's Republic of China

E-mail: tangzhifeng@zju.edu.cn (Z Tang)

Received 21 June 2018, revised 14 August 2018

Accepted for publication 22 August 2018

Published 20 September 2018



Abstract

Switch rails are indispensable components of high speed railway systems, which have stringent nondestructive testing requirements owing to the severe operating conditions. In this article, an ultrasonic guided wave method is proposed for defect detection and localization using independent component analysis (ICA). The temperature effect is included in the data matrix by a random selection of the signals measured at different temperatures. A damage index named the average standard Euclidian distance (ASED) is used to evaluate the deviations of the test signals from the baseline signals in the feature space consisting of the independent components for the defect detection. Once the defect existence is found, defect localization is conducted by another ICA-based decomposition of a new data matrix with additional test signals for the same defect. Independent components whose coefficient vectors show a high correlation with the standard step change vector are chosen to construct the ICA-based residual signal. Then the time instance and location of the defect is determined by observing the first very high peak occurring in the residual signals. A detectability index for defect location (DIDL) is proposed. Experimental validations are performed for the defects on the foot and web of a switch rail. The results of the ASED curves clearly indicate the existence of artificial defects, and the ICA-based residual signals show the location of the defects. The proposed method is found to be superior to conventional methods such as simple baseline subtraction and optimal baseline subtraction regarding the DIDL.

Keywords: switch rails, guided wave monitoring, Independent component analysis, ICA-based residual signals, detectability index for defect location, Standard step change vector, SAFE analysis

(Some figures may appear in colour only in the online journal)

1. Introduction

Switch rails are indispensable components of high speed railway systems for changing the tracks of trains. According to the International Union of Railways, the total mileage of the high-speed railways was more than 30000 kilometers

worldwide in 2016 [1]. There are tens of thousands of switch rails in the railway systems. Because of the complex and harsh working conditions, various defects can occur in the switch rails, becoming hidden hazards. The structural damage and malfunction of a switch rail in service may cause catastrophic accidents such as derailments and train collisions. Therefore,

switch rails require stringent inspection for the long-term and high-level safety. As shown in figure 2(a), the cross-section of a switch rail is not regular and also varies along the longitudinal direction. The cross-sectional variations of the foot and web are mainly within the heel of the switch rail, while the rail head gets sharper along the length. There are several through holes with different diameters distributed non-equidistantly in the rail web. Owing to the structural complexity of switch rails, the defect detectability of conventional non-destructive testing technologies based on ultrasonic [2], magnetic flux leakage [3] or eddy currents [4] is limited to a certain extent. Furthermore, during the operation of railway systems, there is little time available for switch rail inspection, making the conventional methods not applicable for the low working efficiency of testing point by point. Therefore, it is highly urgent and desirable to develop new methods for monitoring the switch rail structure online (accomplished by computers automatically without the intervention of people).

Ultrasonic guided wave methods have been proven to have tremendous potential in the inspection of structures having long and slender dimensions [5–8], and they have been widely used to inspect pipelines [9–12], plates [13–16], rods [17], cables [18], and rails [19–21]. In guided wave testing, a transducer is typically installed at a location to inspect the regions on both sides, and subsequently it is moved to the next location. Even at a given location, the measured signal can be easily affected by the environmental factors and human operations. For example, signals have a high probability of changing even if a transducer is reinstalled by different operators even at the same location. Furthermore, for a structure with geometric changes such as welds, side branches, and holes, the guided waves reflected from the defects will be mixed with those from the geometric changes, making the defects hard to detect. For the past few years, guided waves have been increasingly applied in structural health monitoring (SHM). With permanently installed transducers, the effect of human operations can be significantly reduced, and the newly measured signals can be compared with the baseline signals acquired when the waveguide (i.e. the switch rail in this study) is undamaged.

Many research studies on the damage detection methods using guided wave signals have been reported in recent years [22–34]. In the early years, the residual signals acquired by subtracting the baseline signals from the test signals were analyzed [22]. Then, envelopes rather than the original signals were used for the baseline subtraction (i.e. simple baseline subtraction (SBS) in this study) to improve the signal-to-noise ratio [23]. However, it hardly contributes in the elimination of the overall changes caused by the environmental factors. Temperature variations has been found to make the phases of the acquired signals shift by affecting the mechanical properties of the waveguides, leading to changes of wave velocities and waveguide lengths. The temperature compensation considers building a large database for the baseline signals acquired at different temperatures. Then the best fitting baseline signal to the test signal is selected for the subtraction as in the optimal baseline subtraction (OBS) [24, 25]. Two other methods often used for the compensation of the temperature

effect are the baseline signal stretch (BSS) [26] and local temporal coherence (LTC) [27]. The performance of the above two methods is limited without the consideration of environmental factors besides the temperature.

Recently, feature space decomposition technologies were introduced for the signal processing of guided waves. The baseline signals and test signals are decomposed into the same space so that the components affected by different factors may be separated. The representative methods are the principal component analysis (PCA) [28–30] and the singular value decomposition [31, 32]. These methods focus on the defect detection without localization. There are some other methods based on support vector machine (SVM) [33] or neural networks [34]. Such methods use features extracted from the baseline signals as the training patterns, and equivalent features from the test signals as the test patterns for determining whether they are of the same type. The key for the successful application of those methods is obtaining the features sensitive for the defects but not to the benign environmental changes, which is often difficult in practical applications.

Recently, another method named independent component analysis (ICA) is being used for signal decomposition [35–39]. The main difference between the PCA and ICA is that the extracted principle components (PCs) are statistically uncorrelated and a limited number of PCs with large eigenvalues that are related to the main characteristics are generally used for the signal analysis. However, the components extracted from ICA are independent and a larger number of independent components (ICs) are used, making it easier to identify the slight changes in the test signals. Hence, ICA may be more practical to employ for applications involving high-order statistical properties such as local defects.

In this article, a method based on ICA is proposed for switch rail monitoring using guide waves. In section 2, algorithms for the defect detection and localization are developed. First, the existence of defects is determined by ICA on a data matrix consisting of randomly selected baseline signals and the latest test signal. Once the existence of defects is found, localization of the defects is performed by a second ICA on a new data matrix consisting of the baseline signals and additional numbers of test signals. ICs whose coefficient vectors have step changes (values hop from one level to another) are used to detect the time instance of the defects, from which the location can be identified. In section 3, the wave mode and excitation frequency selection based on the semi-analytical finite element (SAFE) analysis with the whole typical cross section of the switch rail are carried out for the preliminary investigation. Experimental validations conducted with several kinds of defects inflicted on the narrow side of the foot and the web of a switch rail are presented. A damage index named the average standard Euclidian distance (ASED) is used to detect the existence of a defect. Then the localization of the defect is achieved using the ICA-based residual signals. The performance of the proposed ICA-based method for defect localization is discussed in comparison with that obtained by two conventional methods such as SBS and OBS. Conclusions follow in section 4.

2. Defect detection and localization using guided waves

2.1. Data preprocessing

There are generally two stages in structural health monitoring using guided waves. In the first stage, maximal baseline signals without defects are collected under various environmental conditions, while the structural integrity of the waveguide (i.e. switch rail in this study) is confirmed. The second stage is real monitoring, in which each acquired test signal is compared with the baseline signals to evaluate the structural variations (defects) in the waveguide. Preprocessing of the raw signals is generally necessary to eliminate the mean deviation and normalize the amplitudes of the signals before constructing a data matrix for ICA. For guided wave signal $x(t)$, elimination of the mean amplitude deviation can be performed as

$$\tilde{x}(t) = x(t) - \frac{1}{T} \int_0^T x(t) dt \quad (1)$$

where T is the time length of the signal. Normalization can be performed as

$$\hat{x}(t) = \tilde{x}(t) / \sqrt{\frac{1}{T} \int_0^T \tilde{x}(t)^2 dt}. \quad (2)$$

It has been proved that considering the envelopes of the signals can reduce the effect of the slight phase migration and improve the signal-to-noise ratio [23]. In this study, Hilbert envelopes are used [40], which are given as

$$x_e(t) = \sqrt{\hat{x}(t)^2 + \left(\frac{1}{\pi} \int_{-\infty}^{+\infty} \frac{\hat{x}(t-\tau)}{\tau} d\tau \right)^2}. \quad (3)$$

2.2. Defect detection

In this study, ICA is used to analyze the guided wave signals. ICA was proposed initially for blind source separation [35, 36]. For example, if there are three independent sound sources ($\mathbf{s}_1^{ss}, \mathbf{s}_2^{ss}, \mathbf{s}_3^{ss}$) distributed in a space, the sound signals ($\mathbf{x}_1^{ss}, \mathbf{x}_2^{ss}, \mathbf{x}_3^{ss}, \mathbf{x}_4^{ss}$) obtained at four other locations in the same space can be regarded as the linear combinations of those sound sources. This relationship can be written as

$$\begin{bmatrix} \mathbf{x}_1^{ss} \\ \mathbf{x}_2^{ss} \\ \mathbf{x}_3^{ss} \\ \mathbf{x}_4^{ss} \end{bmatrix} = \begin{bmatrix} a_{1,1} & a_{1,2} & a_{1,3} \\ a_{2,1} & a_{2,2} & a_{2,3} \\ a_{3,1} & a_{3,2} & a_{3,3} \\ a_{4,1} & a_{4,2} & a_{4,3} \end{bmatrix} \begin{bmatrix} \mathbf{s}_1^{ss} \\ \mathbf{s}_2^{ss} \\ \mathbf{s}_3^{ss} \end{bmatrix} \quad (4)$$

where the superscript ss denotes the sound signals, and equation (4) can be expressed in a matrix form as

$$\mathbf{X} = \mathbf{AS} \quad (5)$$

where \mathbf{X} and \mathbf{S} denote the data matrix and source matrix, respectively, and \mathbf{A} is the mixing matrix, which is generally related to the paths between the receiving locations and sound sources. The problem of blind source separation is

the determination of a method for estimating source matrix \mathbf{S} from the data matrix \mathbf{X} . For the blind source separation in equation (5), ICA is an effective method with the assumption of source independence. The target of ICA is to derive de-mixing matrix \mathbf{W} to extract the source signals that are mutually independent (i.e. ICs). Then, source matrix \mathbf{S} can be obtained as

$$\mathbf{S} = \mathbf{WX}. \quad (6)$$

The algorithm used in this research is called the fast-ICA technique proposed by Hyvärinen [41]. The ICs are extracted based on the maximization of non-Gaussianity, and the convergence speed and stability of the algorithm are optimized. The first step of the algorithm is the centralization and whitening of the data matrix \mathbf{X} . Then, random initial vector \mathbf{w}_1 , whose norm is 1, is taken into the iteration as follow

$$\mathbf{w}_k = E\{\mathbf{X}(\mathbf{w}_{k-1}')^3\} - 3\mathbf{w}_{k-1}, \quad (7)$$

$$\mathbf{w}_k = \mathbf{w}_k / \|\mathbf{w}_k\| \quad (8)$$

where $E\{\cdot\}$ is the mathematical expectation calculation, and $\|\mathbf{w}_k\|$ represents the norm of \mathbf{w}_k . \mathbf{w}_{k-1}' is the transpose of \mathbf{w}_{k-1} . If $|\mathbf{w}_k' \mathbf{w}_{k-1}|$ is not close to 1, the iteration goes on with $k = k + 1$. The final vector \mathbf{w}_k' is one of the columns in de-mixing matrix \mathbf{W} . Details can be found in [41]. Once de-mixing matrix \mathbf{W} is obtained, mixing matrix \mathbf{A} can be evaluated as the generalized inverse of \mathbf{W} .

Data matrix $\mathbf{X}_{m \times n}$ used for the ICA-based defect detection can be expressed as

$$\mathbf{X}_{m \times n} = \begin{bmatrix} \mathbf{x}_1^b \\ \mathbf{x}_2^b \\ \vdots \\ \mathbf{x}_{m-1}^b \\ \mathbf{x}_1^t \end{bmatrix} \quad (9)$$

where $\mathbf{X}_{m \times n}$ consists of $m - 1$ randomly selected baseline signals (n -dimensional row vectors) and the latest test signal, which are preprocessed $x_e(t)$ in equation (3); n is the dimension (the number of sampling time points) of the signal (generally $n \geq m$); and superscripts b and t denote the baseline and test signals, respectively. M -ICs (s_1, s_2, \dots, s_M), which are n -dimensional row vectors, can be extracted from data matrix $\mathbf{X}_{m \times n}$, and $M \leq m$. Each signal in $\mathbf{X}_{m \times n}$ is a superposition of the M -ICs with different coefficients. This relationship can be written as

$$\begin{bmatrix} \mathbf{x}_1^b \\ \mathbf{x}_2^b \\ \vdots \\ \mathbf{x}_{m-1}^b \\ \mathbf{x}_1^t \end{bmatrix} = \begin{bmatrix} a_{1,1}^b & a_{1,2}^b & \cdots & a_{1,M}^b \\ a_{2,1}^b & a_{2,2}^b & \cdots & a_{2,M}^b \\ \vdots & \vdots & \ddots & \vdots \\ a_{m-1,1}^b & a_{m-1,2}^b & \cdots & a_{m-1,M}^b \\ a_{1,1}^t & a_{1,2}^t & \cdots & a_{1,M}^t \end{bmatrix} \begin{bmatrix} s_1 \\ s_2 \\ \vdots \\ s_M \end{bmatrix} \quad (10)$$

where $\langle a_{i,1}^v, a_{i,2}^v, \dots, a_{i,M}^v \rangle$ is the coefficient row vector in feature space s_1, s_2, \dots, s_M for \mathbf{x}_i^v ($v = \begin{cases} b, & i = 1, 2, \dots, m-1 \\ t, & i = 1 \end{cases}$). Different ICs (s_i s) represent the different factors such as

environment noise, temperatures, and defects affecting the signals in $X_{m \times n}$. The benign factors that exist in both the baseline and test signals but unrelated to the defect cannot separate the test signal from the baseline signals because of the random selection of the baseline signals. However, the defects as the affecting factors that only exist in a test signal will make the signal an outlier. The orders of the ICs in the feature space are not the same for each calculation. Thus, a coefficient named the ASEd is used to evaluate the differences in the test signal and baseline signals in the feature space, which is written as

$$\text{ASEd} = \frac{1}{m-1} \sum_{i=1}^{m-1} \left(\frac{1}{M} \sum_{j=1}^M \sqrt{\frac{(a_{1,j}^b - a_{1,j}^t)^2}{\sigma_j^2}} \right), \quad (i = 1, 2, \dots, m-1) \quad (11)$$

where σ_j is the standard deviation of the coefficients for the j th IC: $a_{1,j}^b, a_{2,j}^b, \dots, a_{m-1,j}^b$ and $a_{1,j}^t$. ASEd can be evaluated for a series of test signals, producing an ASEd curve. Then the existence of the defects can be detected by observing the step changes in this curve.

2.3. Defect localization

The ASEd curve in equation (11) cannot provide information of the defect location. In this study, a method is proposed for the defect detection by constructing a new data matrix employing randomly selected l -baseline signals along with the k -test signals under the same defect condition as

$$X_{(l+k) \times n} = \begin{bmatrix} \mathbf{x}_1^b \\ \mathbf{x}_2^b \\ \vdots \\ \mathbf{x}_l^b \\ \mathbf{x}_1^t \\ \mathbf{x}_2^t \\ \vdots \\ \mathbf{x}_k^t \end{bmatrix}. \quad (12)$$

The data matrix can be decomposed similar to equation (10) using the fast-ICA technique. For each extracted IC s_j ($j = 1, 2, 3, \dots, M_2$; $M_2 < l+k$), the coefficient vector for the j th IC can be written as

$$\mathbf{A}_j = \begin{bmatrix} a_{1,j}^b \\ a_{2,j}^b \\ \vdots \\ a_{l,j}^b \\ a_{1,j}^t \\ a_{2,j}^t \\ \vdots \\ a_{k,j}^t \end{bmatrix}. \quad (13)$$

To obtain the ICs related to the defects whose coefficient vectors have step changes, the correlation coefficients between

the coefficient vectors of the ICs and standard step change vector \mathbf{V}^{ssc} are used, which is defined as

$$\mathbf{V}^{\text{ssc}} = \begin{bmatrix} 0 \\ 0 \\ \vdots \\ 0 \\ 1 \\ 1 \\ \vdots \\ 1 \end{bmatrix} \quad (14)$$

Because the signs of the ICs are uncertain, the absolute value of the correlation coefficients are used for the selection of the ICs as

$$r(\mathbf{A}_j, \mathbf{V}^{\text{ssc}}) = \left| \frac{\sum_{i=1}^{l+k} (a_{i,j} - \bar{A}_j) (V_i^{\text{ssc}} - \bar{V}^{\text{ssc}})}{\sqrt{\sum_{i=1}^{l+k} (a_{i,j} - \bar{A}_j)^2} \cdot \sum_{i=1}^{l+k} (V_i^{\text{ssc}} - \bar{V}^{\text{ssc}})^2} \right| \quad (15)$$

where $a_{i,j}$ is the i th element of \mathbf{A}_j , and \bar{A}_j and \bar{V}^{ssc} denote the average values of the elements of $\mathbf{A}_{(l+k),j}$ and \mathbf{V}^{ssc} , respectively. All the ICs are sorted according to the absolute values of the correlation coefficients (r) in a descending order such as $\{\tilde{s}_1, \tilde{s}_2, \dots, \tilde{s}_{M_2}\}$. The related coefficient vectors are $\{\tilde{\mathbf{A}}_1, \tilde{\mathbf{A}}_2, \dots, \tilde{\mathbf{A}}_{M_2}\}$. In this study, ICA-based residual signal x_R^{ICA} is used for the defect localization as

$$x_R^{\text{ICA}} = \sum_{j=1}^w \left(\frac{1}{k} \sum_{i=l+1}^{l+k} \tilde{A}_{i,j} - \frac{1}{l} \sum_{i=1}^l \tilde{A}_{i,j} \right) \tilde{s}_j \quad (16)$$

where w is the number of selected ICs, which can be determined based on the values of correlation coefficient r with a threshold. The residual signal in equation (16) has high peaks (not troughs) around the defect location and low values elsewhere. The peak values originate from the use of the Hilbert envelopes of the signals.

The algorithm and workflow are shown in figure 1. The main steps are explained below.

Step 1: a data matrix with several randomly selected baseline signals and the latest test signal is constructed, and signal preprocessing is conducted.

Step 2: ICA of the data matrix for the ICs and their coefficient vectors is performed.

Step 3: the ASEd curve is calculated, and the step changes are examined for the defect detection. Otherwise, the process returns to step 1.

Step 4: a new data matrix is conducted with several randomly selected baseline signals and test signals for the defect localization, and the signals are preprocessed.

Step 5: ICA is used to obtain the ICs for the new data matrix.

Step 6: the correlation coefficients between the coefficient vectors of the ICs and the standard step change vector \mathbf{V}^{ssc} are calculated.

Step 7: the ICs are sorted in the descending order of the correlation coefficients, and ICA-based residual signals are constructed for defect localization using ICs with correlation coefficients larger than the threshold. The defect location can

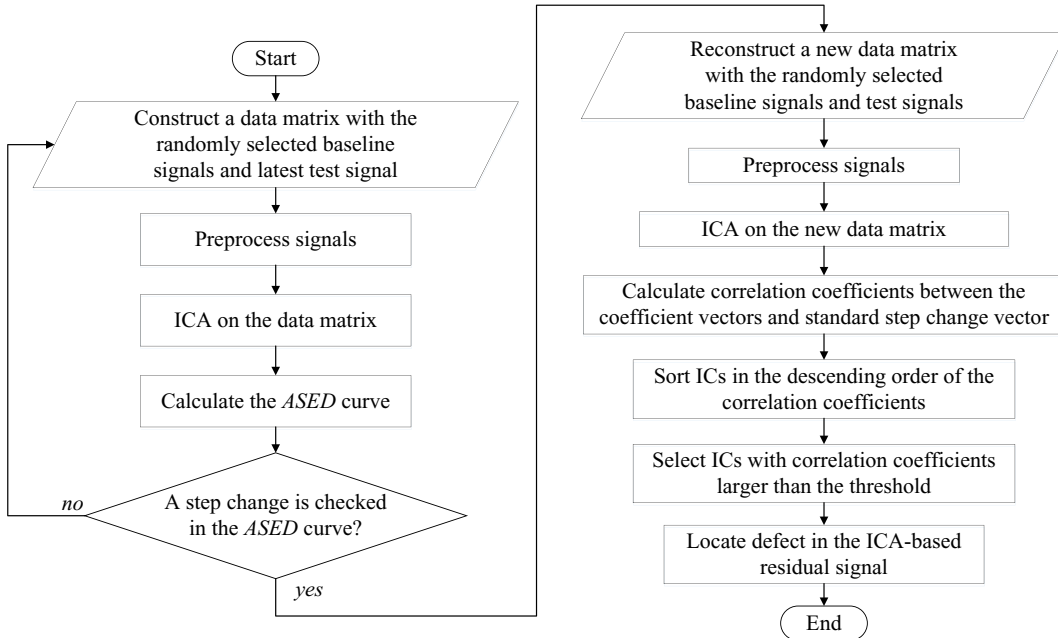


Figure 1. Flow diagram of the proposed algorithm.

be determined by the position of the apparent high peak (not trough) appearing first in the residual signal.

3. Experimental study for defect detection and localization

3.1. Preliminary numerical analysis

The switch rail for the experiments is a 50AT rail with a length of 4.58 m [42]. As shown in figure 2, the cross-section of the switch rail at the heel end has the same shape as the regular rail for the connection (A–A), and it becomes a typical cross-section (B–B) with short height and a large width to endure the lateral forces. The switch rail has a varying cross-section along the longitudinal direction and twelve through holes with different diameters in the web.

The excitation frequency is selected based on the dispersion curves from the semi-analytical finite element (SAFE) analysis for a typical uniform rail cross-section and the preliminary experimental investigation [43]. It should be mentioned that the dispersion curves and wave modes are calculated in Matlab (R2016b, MathWorks) and COMSOL Multiphysics (5.2, COMSOL, inc), respectively. At first, SAFE analysis is carried out with a rail cross-section (B–B), as in figures 2(b) and 6(a). There are 1264 elements with the dimensions between 0.0435 mm–9.72 mm in the mesh grids as in figure 6(a), which were generated by COMSOL with free triangles. The material properties for the rail are taken as: density $\rho = 7850 \text{ kg m}^{-3}$, Young's modulus $E = 210 \text{ GPa}$, and Poisson's ratio $\mu = 0.28$. The dispersion curves for group velocity obtained are shown in figure 6(b).

A frequency range of 50–100 kHz is selected for the experimental investigation, because it is found that large dispersive wave modes exist in low frequencies and large numbers of modes with complexity are in high frequencies. Modes A

and B are found with wave structures (shown in figure 6(b)), whose displacements are mainly distributed in the edge foot and web of the switch rail, respectively. It should be noted that systematic naming rules for wave modes in switch rails have been seen so far, mode A and B are similar to the anti-symmetrical Lamb waves, if the foot and web are treated as plates. Finally the excitation frequency is selected as 65 kHz, at which the largest reflected wave packets from the switch rail ends were obtained in the experiments with a series of frequencies (50, 55, 60, 65, 70, 80, 90, and 100 kHz). Group velocities of Modes A and B by SAFE at 65 kHz are 3.110 and 3.133 km/s, respectively.

3.2. Experimental setup

Two piezoelectric transducers are installed on the narrow side of the rail foot (channel 1) and the rail web (channel 2) by the epoxy coupling at the same location 0.94 m from the heel of the switch rail to detect the local defects imposed on the rail foot and web at three locations, which are 1.5 m, 2.0 m, and 2.5 m from the transducers as exhibited in figures 2–5. The transducers were used both as actuators and sensors. The transducers used in the experiments are sandwich piezoelectric transducers, the diameter of piezoelectric chip is 10 mm and the height of the whole transducer is 20 mm as depicted in figure 3(c). The transducers are unable to control the propagation direction of the guided waves.

The excitation signal used in this study is a tone-burst signal, which is acquired by filtering a sinusoidal signal of one cycle with a Hanning window as in figures 7(a) and (b). Excitation signals with multiple cycles may make the wave packets in the received signals very wide because of the residual vibration of the piezoelectric transducers, reducing the time resolution of the received signals. The sample rate is 1 MHz. A temperature sensor was used to record the temperature of the switch rail

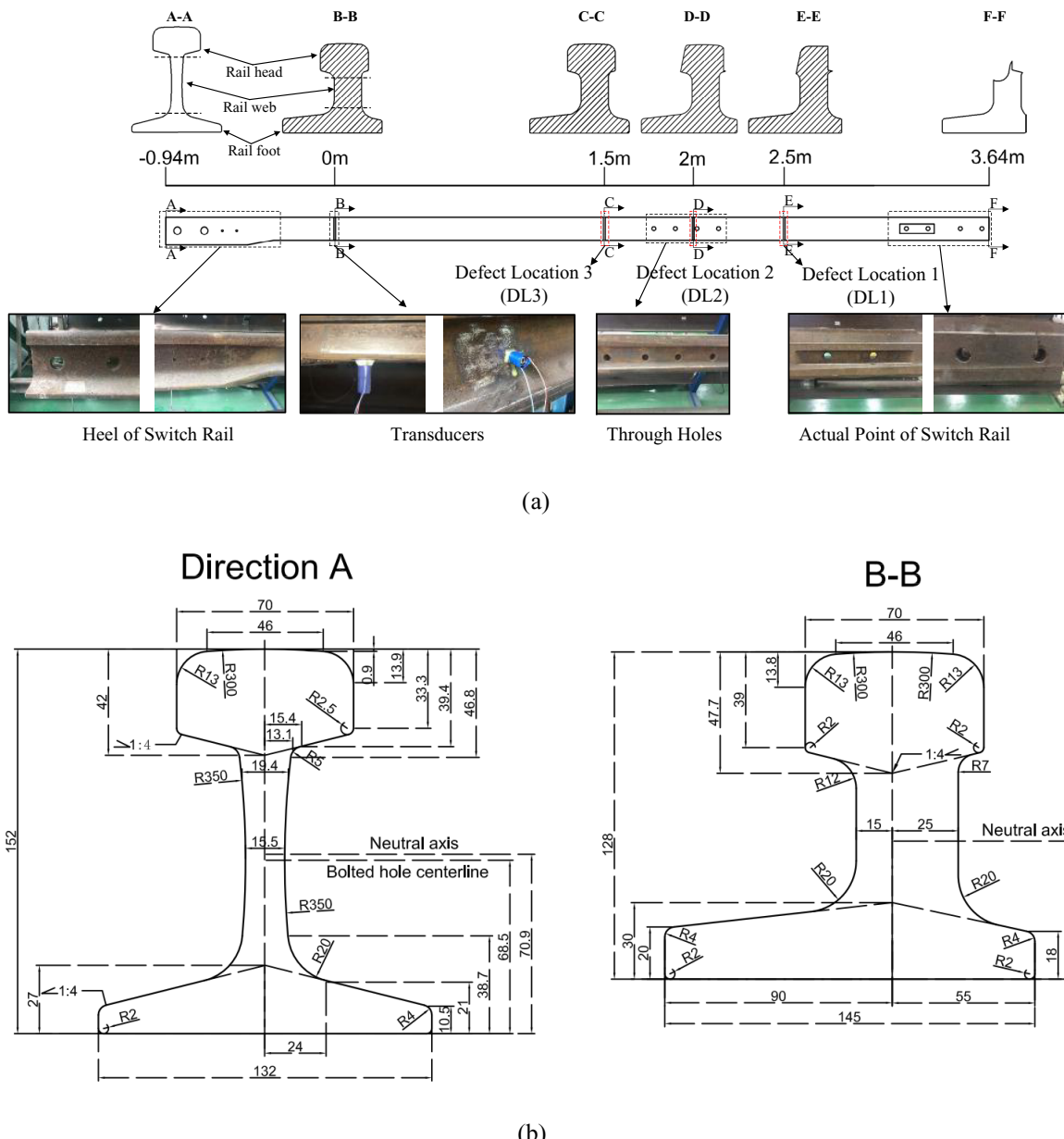


Figure 2. Test structure of a switch rail with artificial defects at three locations: (a) varying cross-sections along the rail and (b) dimensions of typical cross-sections (mm). The static moment of the cross section is zero at the neutral axis; the bolted hole centerline denotes the location of the through hole in the rail web.

with the probe installed fixedly near the transducers as shown in figure 3(d). It should be noted that the temperature variations were not large along the rail structure and during the laboratory experiments: 10.5 °C–22.7 °C. The schematic and photos of the guided wave monitoring system are shown in figure 3.

The first monitoring experiment was conducted on the narrow side of the switch rail foot. Three cases of defects were considered: Mass Scatterer 1 at Defect Location 1 (DL1), Cut 1 and Expanded Cut 1 at Defect Location 2 (DL2), as shown in figures 2 and 4. Initially, baseline signals without the imposed defects were collected 800 times. Then the test signals were collected for various cases with and without defects, as described in table 1. Mass Scatterer 1 introduced at DL1

causes an increase in the cross-sectional area of the rail by 900 mm^2 ($30 \times 30\text{ mm}^2$). Cut 1 introduced at DL2 causes a reduction in the cross-sectional area by 66 mm^2 ($22 \times 3\text{ mm}^2$), whereas Expended Cut 1 causes a cross-section reduction by 110 mm^2 ($22 \times 5\text{ mm}^2$). The number of test signals and temperature range over time of each damage case are presented in table 1.

For the experiments on the rail web, two types of defects were caused at Defect Location 3 (DL3), as in figures 2 and 5. Mass Scatterer 2 results in an additional cross-sectional area of 600 mm^2 ($30 \times 20\text{ mm}^2$), whereas Cut 2 reduces the cross-section of 102 mm^2 (38 mm in length, maximum depth is 4 mm, a part of the circle with the diameter 94 mm). The number of signals and temperature range over time of each

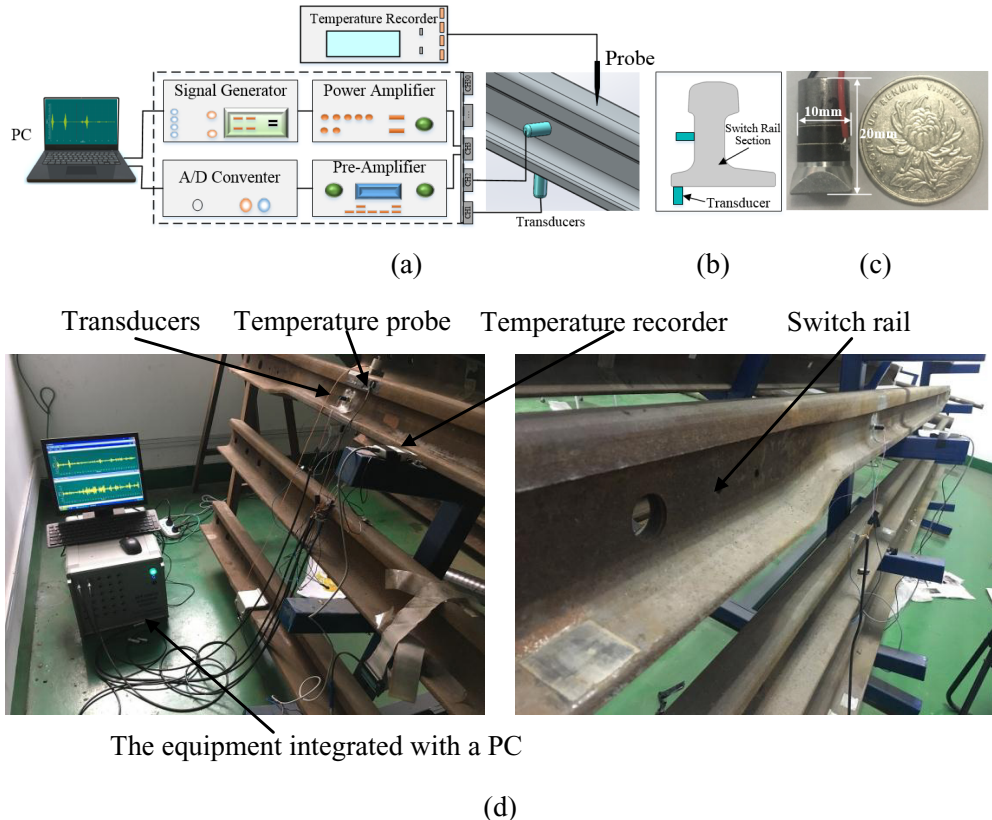


Figure 3. Experimental setup: (a) multichannel guided wave monitoring system; (b) transducers installation on the narrow side of the rail foot and rail web; (c) sandwich piezoelectric transducer. (d) Photos of the experimental system.

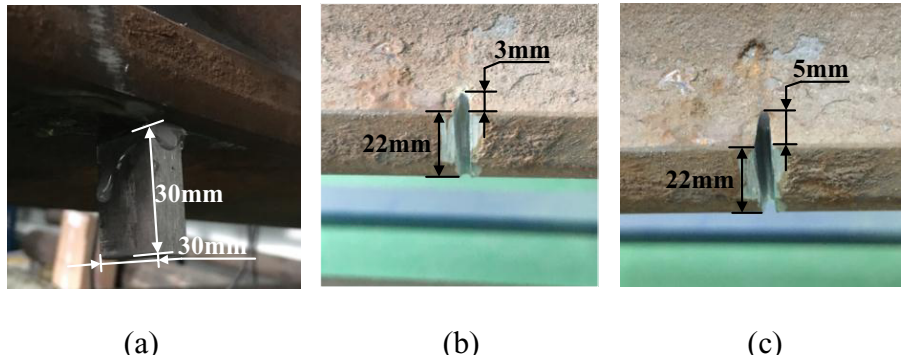


Figure 4. Artificial defects on the narrow side of the rail foot: (a) mass scatterer 1 at DL1, (b) cut 1 at DL2, and (c) expanded cut 1 at DL2.

damage case are listed in table 2. It should be mentioned that the widths of the mass scatterers and cuts are 10 mm and 2 mm, respectively. The temperature ranges of the test signals are within the temperature ranges of the baseline signals.

3.3. Defect existence using ICA-based ASEd curves

Typical original signals collected before and after the introduction of Mass Scatterer 1 on the narrow side of the rail foot are shown in figure 8(a), and those with and without Mass Scatterer 2 on the rail web are in figure 8(b). It should be noted that the measured time signals in figure 8 are converted to distance signals using the estimated group velocities. The relationship between the distance (d) and flight time

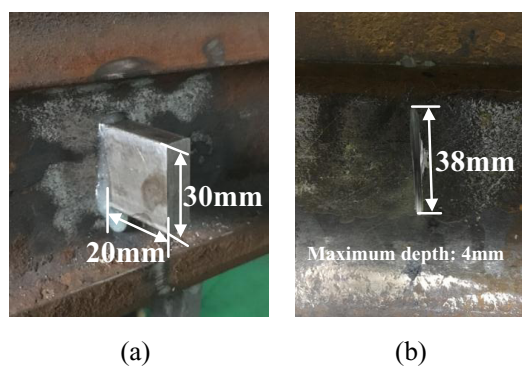


Figure 5. Artificial defects on the rail web: (a) Mass Scatterer 2 at DL3, and (b) cut 2 at DL3.

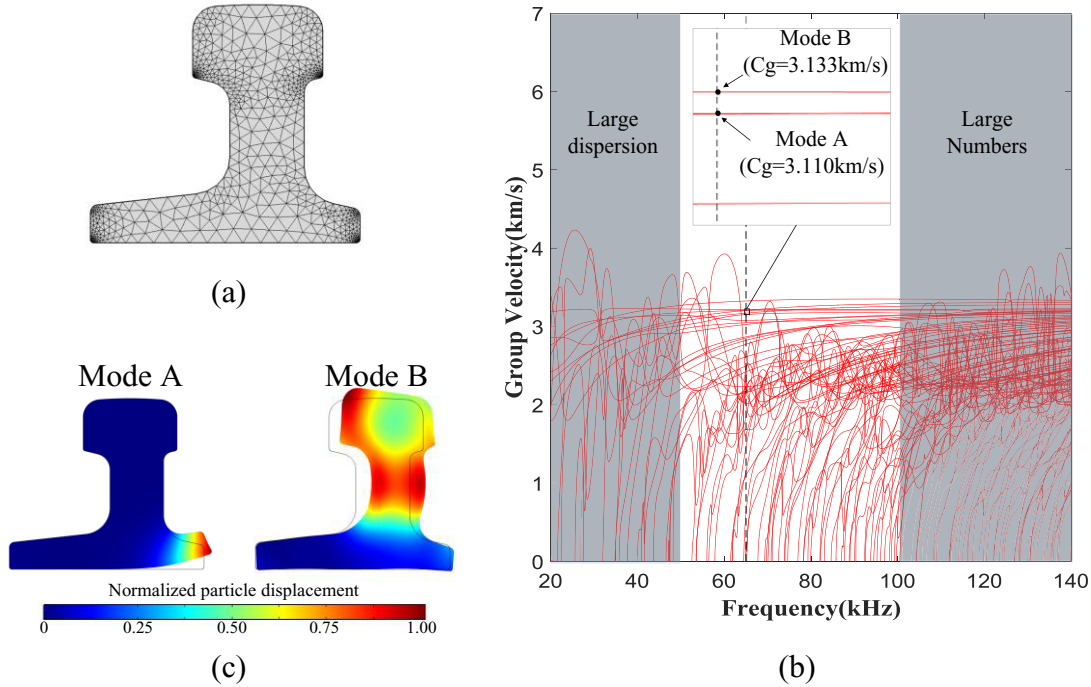


Figure 6. SAFE-based dispersion curves: (a) SAFE mesh grids of a rail cross section B-B; (b) group velocity dispersion curves; (c) local deformation modes.

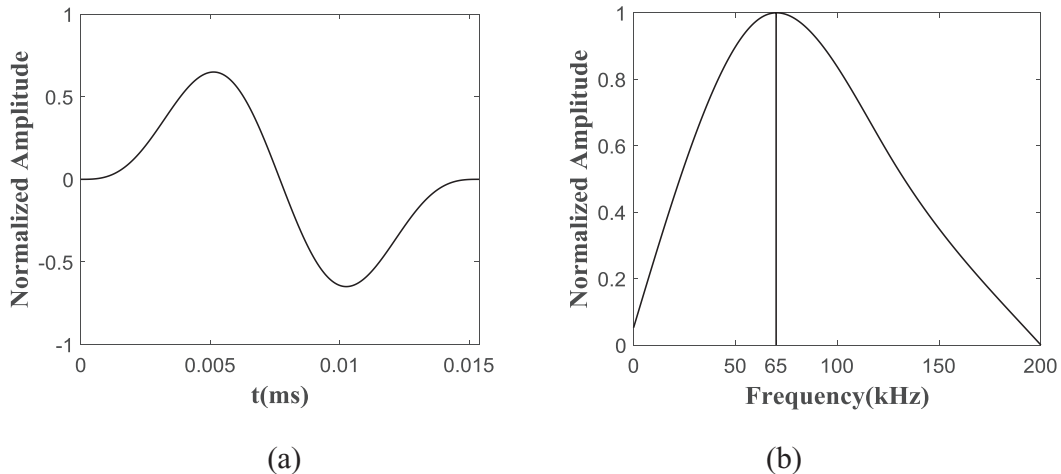


Figure 7. Excitation signal: (a) time excitation signal; (b) amplitude spectrum of the excitation signal.

Table 1. Signal collection on the narrow side of the rail foot.

Defect cases	Status	Numbers of signals	Temperature range (°C)
F1	Baseline collection	800	16.5–22.7
F2	No defect	55	19.7–20.8
F3	Mass Scatterer 1 introduced at DL1	252	17.2–21.8
F4	Mass Scatterer 1 removed at DL1	198	18.4–20.8
F5	Cut 1 introduced at DL2	382	18.2–20.3
F6	Cut 1 expanded at DL2	250	18.5–19.8

(t) is $d = vt/2$ considering a round trip of the reflected wave. The distance signals are more convenient for the localization of defects. Table 3 shows the estimated group velocities of the wave modes in the narrow side of the rail foot (2720.7 m s^{-1}) and the rail web (2458.6 m s^{-1}), which were determined

experimentally based on reflected waves from the ends of the switch rail (matching the wave packets in the signals and the geometric changes in the switch rails with SAFE speeds and experience). Significant differences (12.5%–21.5%) between the speeds by experiments and SAFE analysis may be caused

Table 2. Signal collection on the switch rail web.

Defect cases	Status	Numbers of signals	Temperature range (°C)
W1	Baseline collection	1000	10.5–14.5
W2	No defect	141	12.1–14.0
W3	Mass Scatterer 2 introduced at DL3	312	11.6–14.5
W4	Mass Scatterer 2 removed at DL3	166	12.2–14.0
W5	Cut 2 introduced at DL3	150	11.2–12.6

Table 3. Speed estimation using the reflected signals from the ends of the switch rail.

Region	Feature	Arrival time (ms)	Actual distance (m)	Estimated speed (m s^{-1})	SAFE speed (m s^{-1})	Difference in speed (%)
foot	Heel	0.691	0.94	2720.7	3110	12.5
web	Actual point	2.961	3.64	2458.6	3133	21.5

Note: 1. Estimated speed = $2 \times \text{Actual distance}/\text{Arrival time}$; 2. SAFE speeds are calculated using a uniform rail cross-section (B–B).

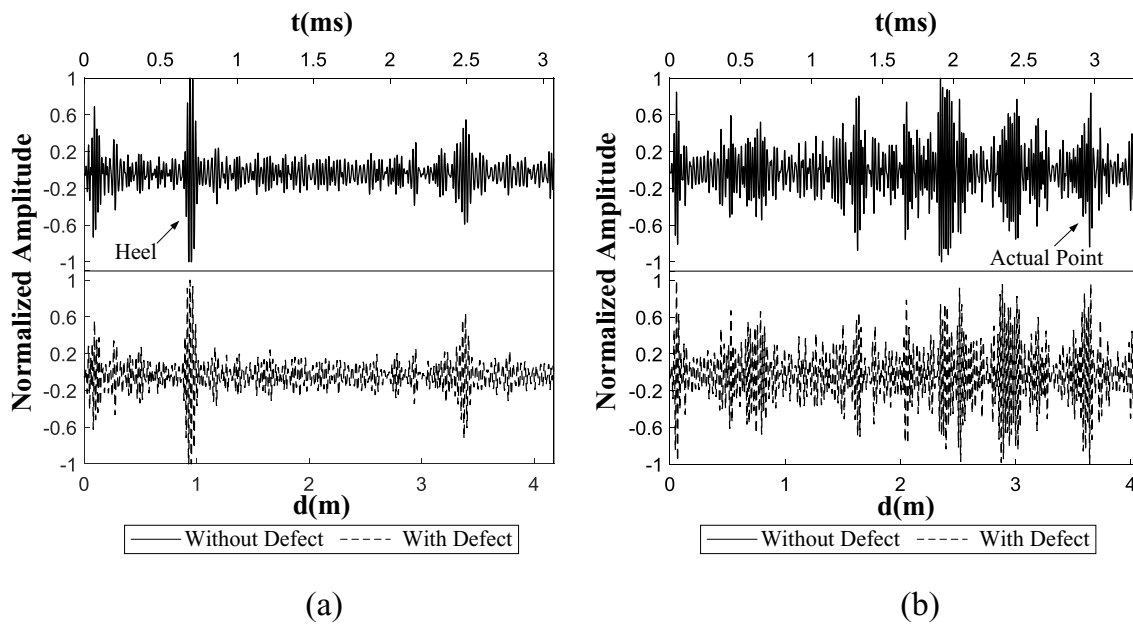


Figure 8. Typical original signals: (a) at the narrow side of the rail foot with and without effect of Mass Scatterer 1 at DL1; (b) on the rail web with and without effect of Mass Scatterer 2 at DL3.

by the cross-section variation in the switch rail. With the original signals, it is very difficult to discriminate the defect existence and obtain valuable information of the defect location. Therefore, advanced signal processing is necessary.

In the experiments for the defect detection on the narrow side of the switch rail foot, 120 baseline signals were randomly selected to construct a data matrix with the latest collected test signal. All the signals were preprocessed: $x_e(t)$ as in equation (3). ASED and temperature variations along the test cases are presented in figure 9. ASED represents the average deviation between the test signal and baseline signals for each test case. The ASED curve exhibits abrupt step changes at the instants of the introduction and removal of Mass Scatterer 1. Similarly, the ASED curve shows a slight change with the introduction of cut 1 and a significant step change on the expansion of cut 1.

The results of monitoring the switch rail web are displayed in figure 10. The ASED curve also shows abrupt step changes

at the precise instants of the introduction and removal of Mass Scatterer 2. The defect area of cut 2 is much smaller than the additional cross-sectional area of Mass Scatterer 2, but cut 2 also causes the ASED to increase. It can be observed that the instants and levels of the structural changes are clearly shown as step changes in the ASED curve, which is affected little by the temperature variation.

Comparisons between ASEDs for signals processed with and without the ICA method are also carried out, as shown in figures 9 and 10. The curves without the ICA method successfully denote large cross-sectional changes like the introduction and removal of the mass scatters and a large cut. However, it fails to test small defects. The signals used to calculate ASEDs can be regard as vectors with thousands of dimensions, and changes of several dimensions caused by small defects may be covered up by the random variations of the other dimensions. But, the effect of small defects raises after the dimensionality reduction achieved by the ICA method.

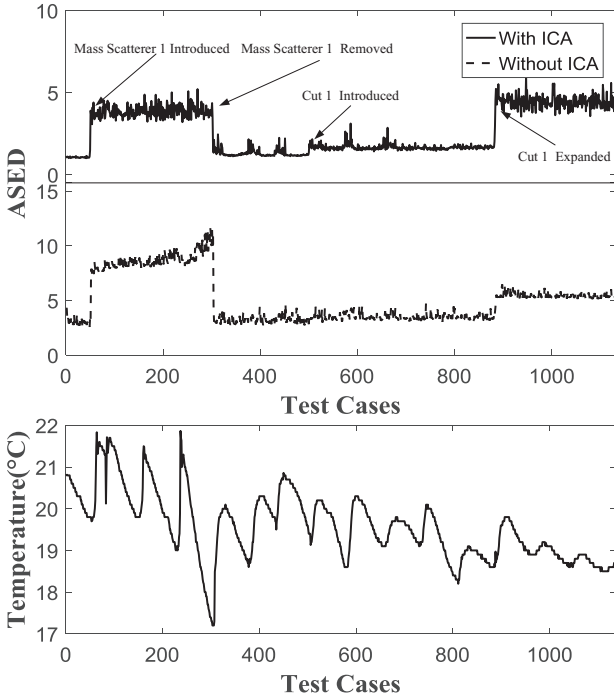


Figure 9. ASEEDs and temperature variations during the tests with various damages to the rail foot.

3.4. Defect localization using ICA-based residual signals

Localization is a basic requirement for defect detection with guided waves. A step change occurring in an ASEED curve is an indication of a defect. Because defects impact only the corresponding test signals, the ICs with coefficient vectors similar to the standard step change vector (\mathbf{V}^{ssc} in equation (14)) are more related to the defects. To extract the defect-related ICs by ICA, 120 randomly selected baseline signals and 20 test signals with the same defect were used: i.e. $l = 120$ and $k = 20$ in equation (12). For Mass Scatterer 1, 140 ICs are calculated, and they are sorted by the absolute values of correlation coefficients r in a descending order, which is shown in figure 11(a). In figure 11, IN denotes the IC number sorted by r . Figure 11(b) displays several ICs with different r and their coefficient vectors A_j . ICs with r close to one are supposed to contain more information about the defects, whereas others with r close to zero are not. Different numbers of ICs are selected to construct ICA-based residual signals x_R^{ICA} in equation (16), and the results, of which maximum values are normalized to 1.0, are shown in figure 12. As previously, time signals x_R^{ICA} are converted into space signals using the wave propagation speed. It should be noticed in x_R^{ICA} with $w = 3$ that the first positive wave packet in the solid ellipse represents the direct reflection echo from Mass Scatterer 1. This indicates that the location of Mass Scatterer 1 is 2.75 m from the transducer, corresponding to a 10.0% error compared with the actual distance of 2.50 m. The wave packet within the dotted ellipse at 3.79 m is related to the distance between the heel of the switch rail and Mass Scatterer 1, which causes the guided waves to be reflected twice at two structural changes. The error in this estimation is 10.2% in comparison with the

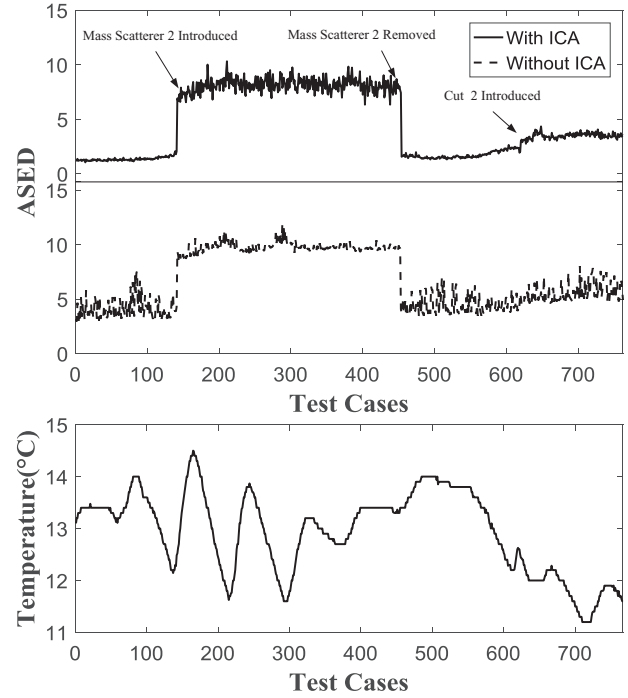


Figure 10. ASEEDs and temperature variations during the tests with various damages on the rail web.

actual distance of 3.44 m. It is noted that the group velocities of the wave modes vary when they are propagating in waveguides with varying cross-sections (i.e. switch rails in this study) [44]. This may be the reason for the above localization errors. An ICA-based residual signal (in equation (16)) may lose the relevant information about the defects if the number (w) of ICs considered is not sufficient (e.g. $w = 1$). However, if numerous ICs are used (e.g. $w = 140$), other wave components from unknown locations will disturb the signal analysis. Therefore, selection of the appropriate number of ICs is important for accurate defect detection. In this study, w is chosen as three using a threshold value of 0.96 for the correlation coefficient r . The results for Mass Scatterer 1 confirm that the proposed method using the standard step change vector can effectively identify the signal variations caused by the defects for localization.

3.5. Comparison with other methods on defect localization

The performance of the present ICA-based residual method (ICAR) is compared with that of two other methods, namely, SBS and OBS. The BSS method was not considered because it is expected to yield similar results to the OBS method with a large base data. The LTC method was also not considered because the temperature was uniform along the rail during the experiments. The SBS method uses only one single baseline signal, which is randomly selected from baseline signals $x_j^b(t)$ for each test signal in this study. The OBS method uses a residual signal based on the optimal baseline signal among baseline data $x_j^b(t)$, which gives least mean square residual δ_{ms} for test signal $x^t(t)$ as

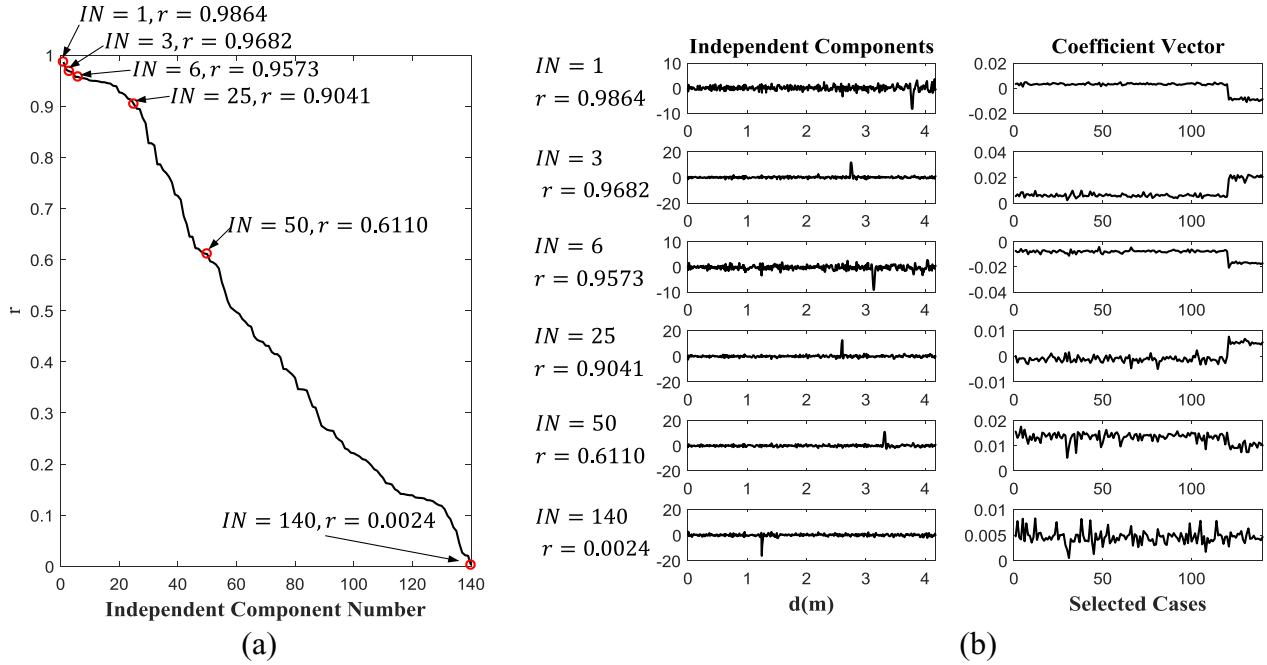


Figure 11. Sorted ICs for a case with Mass Scatterer 1: (a) absolute values of correlation coefficients r ; (b) ICs with different r and their coefficient vectors.

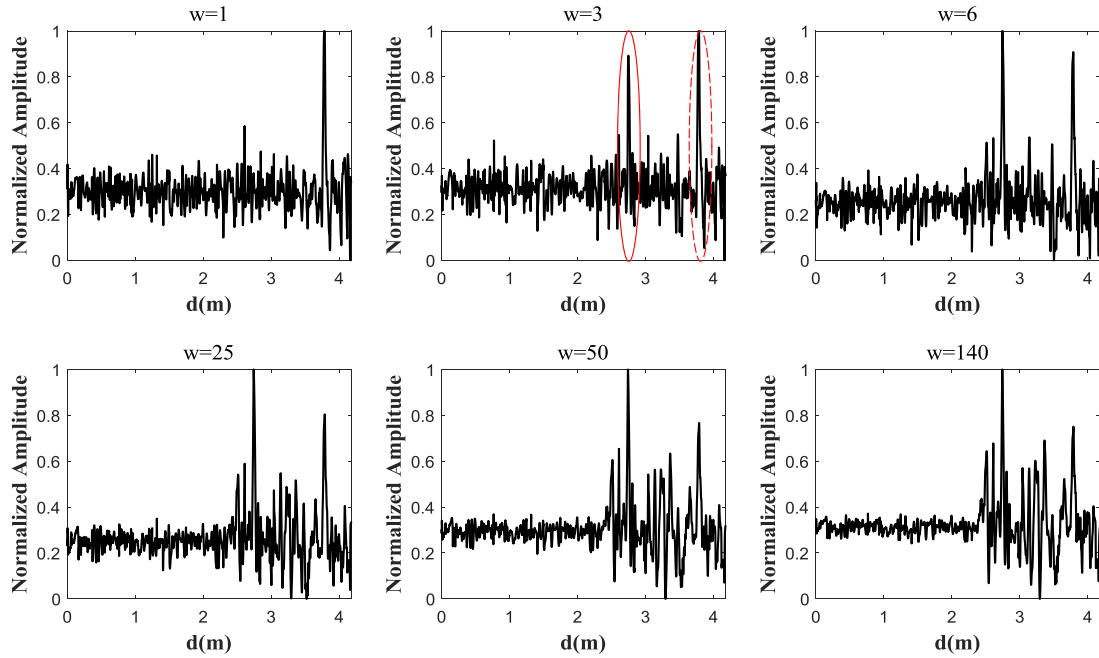


Figure 12. ICA-based residual signals with different numbers (w) of the ICs for the case of Mass Scatterer 1. The wave packet within the solid ellipse represents the direct reflection echo from Mass Scatterer 1. The wave packet within the dotted ellipse represents waves between the heel of the switch rail and Mass Scatterer 1, which are reflected twice.

$$\min_j \delta_{ms} = \left\{ \frac{1}{n} \sum_{i=1}^n (x^t(i) - x_j^b(i))^2 \right\}. \quad (17)$$

The OBS and ICAR methods are compared using the same data. The residual signals obtained are all normalized for waveform comparison, and the results are shown in figures 13 and 14, in which the location of the defect can be identified by the high peak (not trough), as marked by a solid ellipse.

Noted that the troughs after the defect indicate wave reduction owing to the defects, whereas those before the defect are caused by some other effects. It can be observed that for defects with slight cross-section areal changes (cut 1 and cut 2), the performance of the OBS method is barely satisfactory, and localization cannot be achieved without prior-knowledge of the defects. In contrast, the peaks of the ICAR method are more apparent for the defect localization with less distraction, which show significant advantages for small defects. The

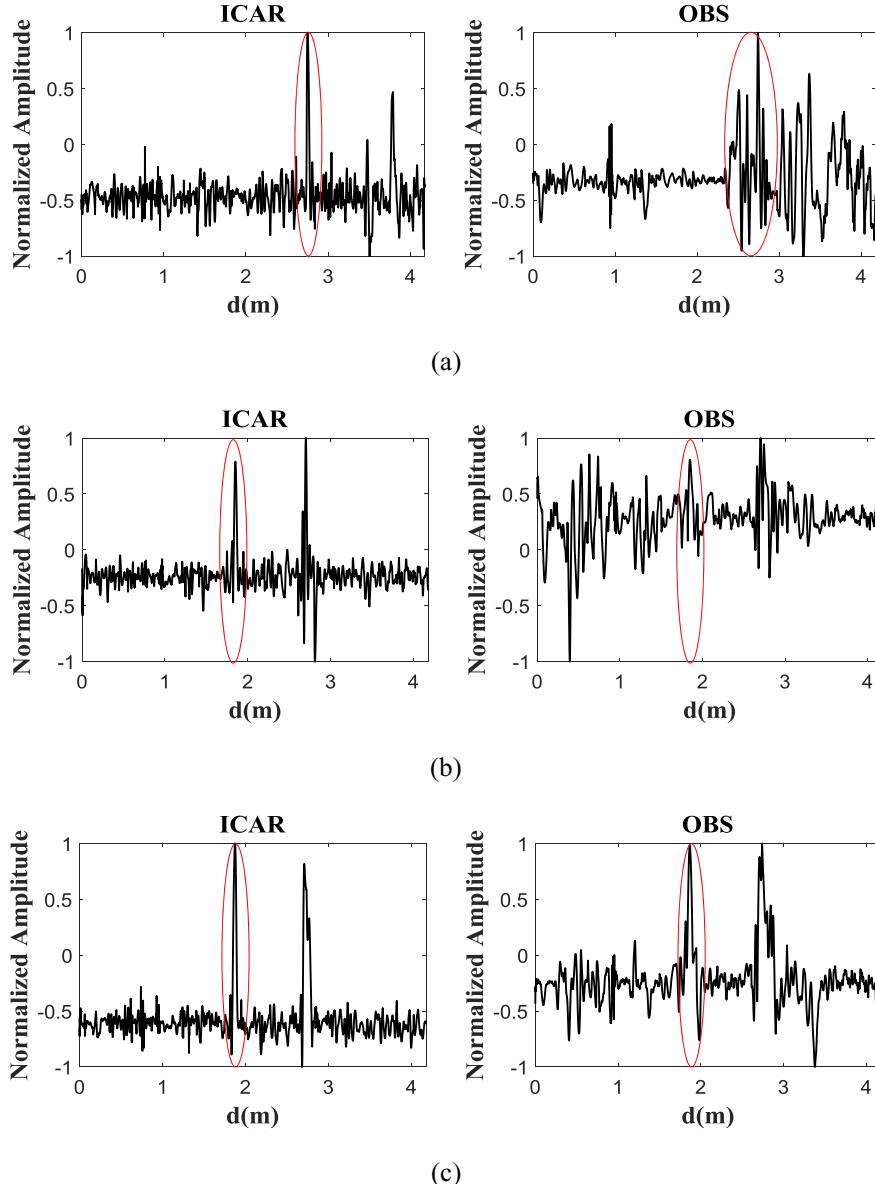


Figure 13. Residual signals for the defects on the rail foot: (a) Mass Scatterer 1 at DL1; (b) cut 1 at DL2; (c) expanded cut 1 at DL2. The wave packets within the solid ellipse represent the direct reflection echo from the defects.

detectability index for defect location (DIDL) is derived in this study as

$$\text{DIDL} = \frac{\|x_{R_{\max}}^a\|}{\|x_{R_{\max}}^a\| + \|x_{R_{\max}}^b\|}; 0 < \text{DIDL} < 1 \quad (18)$$

$$\|x_{R_{\max}}^a\| = \max_i \{x_R(i)\} - \bar{x}_{Rb}; i \in [n_b + 1, n_b + n_a] \quad (19)$$

$$\|x_{R_{\max}}^b\| = \max_j \{x_R(j)\} - \bar{x}_{Rb}; j \in [1, n_b] \quad (20)$$

where n_b and n_a are the numbers of the time steps before and around the defect, and \bar{x}_{Rb} is the mean value of $x_R(t)$ before the defect. In equations (19) and (20), $\|x_{R_{\max}}^a\|$ represents the effect of the defect in a residual signal, whereas

$\|x_{R_{\max}}^b\|$ corresponds to the environment such as temperature and operational loads. The value of the DIDL in equation (18) approaches to one when it is very obvious to detect the peak location in the residual signal. On the other hand, the value less than 0.5 indicates failure in the defect localization.

Estimated defect locations are listed in table 4. By the proposed ICAR, the localization errors for the defects on the web and foot are found to be small (6.00%–12.7%), which may be improved even further by considering the speed changes caused by the cross-sectional variations, as mentioned in section 3.4. The DIDLs of the ICAR method are much higher than those by the OBS method. Particularly for small defects of cut 1 and cut 2, the DIDLs for OBS are found to be less than 0.5, which indicate failure in the defect localization. It has been found that if the localization is successful as in large defect cases with

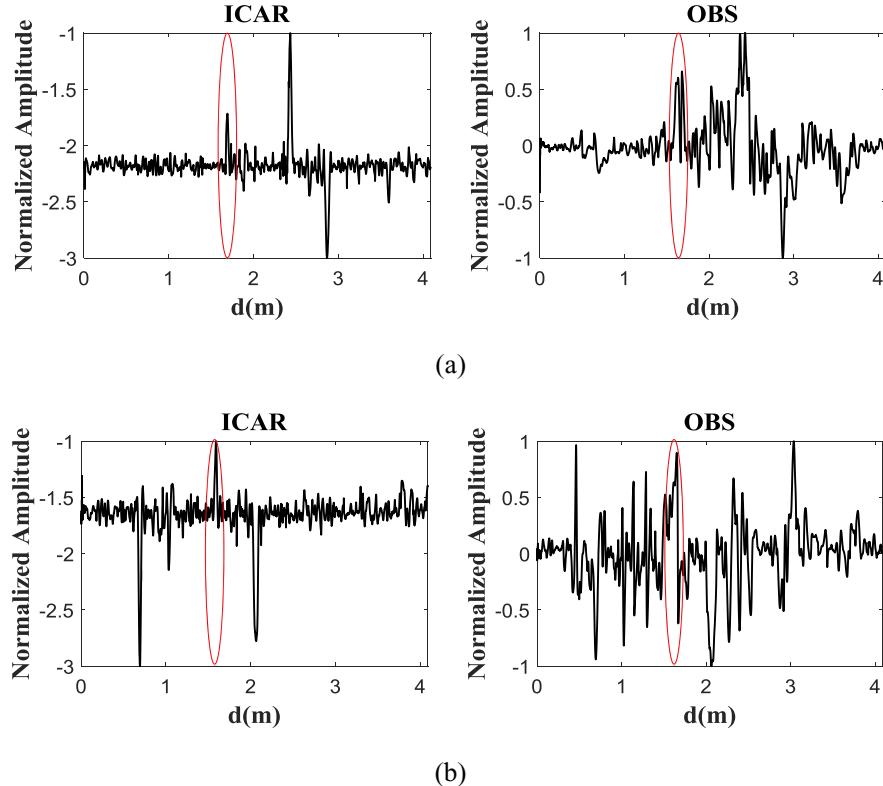


Figure 14. Residual signals for the defects on the rail web: (a) Mass Scatterer 2 at DL3; (b) cut 2 at DL3. The wave packets within the solid ellipse represent the direct reflection echo from the defects.

Table 4. Estimated locations of the defects and detectability index (DIDL).

Defects	Number of signals	Actual distance (m)	Estimated distance (m)					
			ICAR			OBS		
			Value	Error	Std	Value	Error	Std
Mass Scatterer 1 on rail foot	252	2.50 (DL1)	2.75	10.0	0.06	2.75	10.0	0.03
Cut 1 on rail foot	382	2.00 (DL2)	1.85	7.50	0.02	Failure		
Expanded Cut 1 on rail foot	250	2.00 (DL2)	1.87	6.50	0.02	1.87	6.50	0.11
Mass Scatterer 2 on rail web	312	1.50 (DL3)	1.69	12.7	0.04	1.68	12.0	0.01
Cut 2 on rail web	150	1.50 (DL3)	1.59	6.00	0.08	Failure		
DIDL								
ICAR	OBS							
0.786	0.603							
0.820	0.462							
0.823	0.694							
0.838	0.753							
0.665	0.445							

Note: The estimation errors are in percent; the stds denote the standard deviations of the estimated distances. The estimated distances and DIDLs are average values.

mass scatterers and expanded cut, the OBS estimates are similar to those of the proposed ICAR method in both localization errors and standard deviations. The results in figure 15 show that the ICAR method gives the best results with the highest

detectability index (DIDL). The OBS method provides significant improvement in the effect elimination of the environmental factors compared with the SBS method, however both conventional methods fail in the localization of small defects.

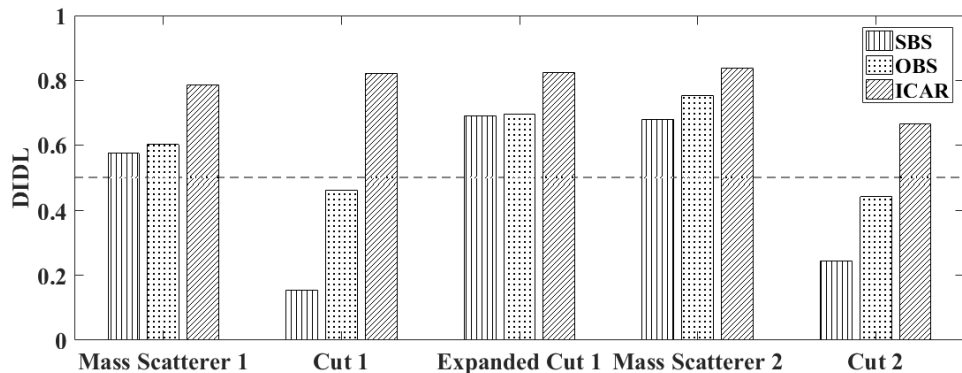


Figure 15. Detectability indices for the defect locations (DIDL) for various defects.

4. Conclusions

A new independent component analysis (ICA)-based method is proposed for the defect detection and localization for a switch rail structure using ultrasonic guided waves. Standard step change vector V^{SSC} is employed to obtain the coefficient vectors of the ICs, for effective extraction of the ICs closely related to the defect. Experimental validation was successfully performed for the detection of the defects on the foot and web of a switch rail. The main findings are summarized as follows:

1. The ASED curves have the ability to determine the occurrence of structural changes caused by local cross-sectional increment (mass scatterer) and damage (cut) in a switch rail. And improvements in denoting small defects can be achieved with the signals processed by the ICA method compared with the raw signals.
2. Defect locations can be identified from the first high peak in the ICA-based residual signals obtained by appropriate number of ICs, whose coefficients are highly correlated with V^{SSC} . The localization errors are found to be fairly small: 6.00%–12.7% for the defects on the foot and web.
3. A detectability index for defect location (DIDL) is devised. The DIDLs by the proposed ICA-based method are found to be much higher than those by two other methods, such as simple baseline subtraction (SBS) and optimal baseline subtraction (OBS). The proposed method can detect the locations of small defects (cut 1 and 2) with high accuracy (with 6.00%–7.5% errors), while the other two conventional methods fail. If the localization is successful as in large defect cases, the localization errors and standard deviations of the OBS methods are found to be similar to those of the proposed method.
4. The semi-analytical finite element (SAFE) analysis has been found to be very effective to determine the preliminary range of the excitation frequency and to identify the wave modes related to the local defects on the foot and web of the rail, which has a varying cross-section.

The ICA-based method is expected to be used effectively for the health monitoring of switch rails in service to minimize the accident, risk, and cost for the maintenance operations. For further study, it is suggested to examine the effects of the accessories installed in a switch rail, larger temperature

variation effect, threshold determination of r for number selection of ICs, DIDL improvement for smaller defects and wave speed variation due to the varying cross-section along the rail.

Acknowledgment

The authors acknowledge the financial supports from the National Natural Science Foundation of China (No.61271084, No.51275454, No.U1709216), the National Key Research and Development Program of China (2018YFC0809000), the Fundamental Research Funds for the Central Universities, and Science and the Technique Plans of Zhejiang Province (2017C01042).

ORCID iDs

Jianjun Wu <https://orcid.org/0000-0001-6054-7364>

References

- [1] UIC 2016 30,000 km of high speed lines in the world (<http://timelines.uic.org/announcement/2015-30-000km-of-high-speed-lines-in-the-world/>) (2016-12)
- [2] Aharoni R, Glikman E and Krug G 2002 A novel high-speed rail inspection system *J. Nondestruct. Test.* **7** 9
- [3] Li Y, Wilson J and Tian G Y 2007 Experiment and simulation study of 3D magnetic field sensing for magnetic flux leakage defect characterisation *NDT & E Int.* **40** 179–84
- [4] Junger M, Thomas H M, Krull R and Rühe S 2004 The potential of eddy current technology regarding railroad inspection and its implementation *Proc. of the 16th World Conf. on Non-Destructive Testing (Montreal, Canada)*
- [5] Rose J L 2011 The upcoming revolution in ultrasonic guided waves *Proc. SPIE* **7983** 798302
- [6] Mijarez R, Gaydecki P and Burdekin M 2005 An axisymmetric guided wave encoded system for flood detection of oil rig cross-beams *Meas. Sci. Technol.* **16** 2265
- [7] Ervin B L and Reis H 2008 Longitudinal guided waves for monitoring corrosion in reinforced mortar *Meas. Sci. Technol.* **19** 055702
- [8] Rizzo P, Marzani A and Bruck J 2010 Ultrasonic guided waves for nondestructive evaluation/structural health monitoring of trusses *Meas. Sci. Technol.* **21** 045701
- [9] Kwun H and Dynes C P 1998 Long-range guided wave inspection of pipe using magnetostrictive sensor

- technology: the feasibility of defect characterization *Proc. SPIE* **3398** 28–35
- [10] Ma J, Lowe M J S and Simonetti F 2007 Feasibility study of sludge and blockage detection inside pipes using guided torsional waves *Meas. Sci. Technol.* **18** 2629
- [11] Wang X, Peter W T and Dordjevich A 2010 Evaluation of pipeline defect's characteristic axial length via model-based parameter estimation in ultrasonic guided wave-based inspection *Meas. Sci. Technol.* **22** 025701
- [12] Chang Y, Zi Y, Zhao J, Yang Z, He W and Sun H 2017 An adaptive sparse deconvolution method for distinguishing the overlapping echoes of ultrasonic guided waves for pipeline crack inspection *Meas. Sci. Technol.* **28** 035002
- [13] Ebrahimkhanlou A and Salamone S 2018 Single-sensor acoustic emission source localization in plate-like structures using deep learning *Aerospace* **5** 50
- [14] Ebrahimkhanlou A and Salamone S 2017 A probabilistic framework for single-sensor acoustic emission source localization in thin metallic plates *Smart Mater. Struct.* **26** 095026
- [15] Ebrahimkhanlou A and Salamone S 2017 Acoustic emission source localization in thin metallic plates: a single-sensor approach based on multimodal edge reflections *Ultrasonics* **78** 134–45
- [16] Ebrahimkhanlou A, Dubuc B and Salamone S 2016 Damage localization in metallic plate structures using edge-reflected lamb waves *Smart Mater. Struct.* **25** 085035
- [17] He C, Sun Y X, Wu B, Wang X Y and Liu Z H 2006 Application of ultrasonic guided waves technology to inspection of bolt embedded in soils *Yantu Gongcheng Xuebao (Chin. J. Geotechn. Eng.)* **28** 1144–7
- [18] Baltazar A, Hernandez-Salazar C D and Manzanares-Martinez B 2010 Study of wave propagation in a multiwire cable to determine structural damage *NDT & E Int.* **43** 726–32
- [19] Rose J L, Avioli M J, Mudge P and Sanderson R 2004 Guided wave inspection potential of defects in rail *NDT & E Int.* **37** 153–61
- [20] Palmer S B, Dixon S, Edwards R S and Jian X 2005 Transverse and longitudinal crack detection in the head of rail tracks using Rayleigh wave-like wideband guided ultrasonic waves *Proc. SPIE* **5767** 70–81
- [21] Zumpano G and Meo M 2006 A new damage detection technique based on wave propagation for rails *Int. J. Solids Struct.* **43** 1023–46
- [22] Lu Y and Michaels J E 2005 A methodology for structural health monitoring with diffuse ultrasonic waves in the presence of temperature variations *Ultrasonics* **43** 717–31
- [23] Croxford A J, Wilcox P D, Konstantinidis G and Drinkwater B W 2007 Strategies for overcoming the effect of temperature on guided wave structural health monitoring *Proc. SPIE* **6532** 65321T
- [24] Konstantinidis G, Drinkwater B W and Wilcox P D 2006 The temperature stability of guided wave structural health monitoring systems *Smart Mater. Struct.* **15** 967
- [25] Clarke T, Simonetti F and Cawley P 2010 Guided wave health monitoring of complex structures by sparse array systems: influence of temperature changes on performance *J. Sound Vib.* **329** 2306–22
- [26] Croxford A J, Moll J, Wilcox P D and Michael J E 2010 Efficient temperature compensation strategies for guided wave structural health monitoring *Ultrasonics* **50** 517–28
- [27] Michaels J E and Michaels T E 2005 Detection of structural damage from the local temporal coherence of diffuse ultrasonic signals *IEEE Trans. Ultrason. Ferroelectr. Freq. Control* **52** 1769–82
- [28] Liu C et al 2012 Robust change detection in highly dynamic guided wave signals with singular value decomposition *2012 IEEE Int. Ultrasonics Symp. (IUS)* (Piscataway, NJ: IEEE) pp 483–6
- [29] Liu C, Harley J B, Bergés M, Greve D W, Junker W R and Oppenheim I J 2014 A robust baseline removal method for guided wave damage localization *Proc. SPIE* **9061** 90611K
- [30] Liu C, Harley J B, Bergés M, Greve D W and Oppenheim I J 2015 Robust ultrasonic damage detection under complex environmental conditions using singular value decomposition *Ultrasonics* **58** 75–86
- [31] Eybooposh M, Bergés M and Noh H Y 2014 Toward characterizing the effects of environmental and operational conditions on diffuse-field ultrasonic guided-waves in pipes *Proc. SPIE* **9061** 90611M
- [32] Eybooposh M, Bergés M and Noh H Y 2015 Nonlinear feature extraction methods for removing temperature effects in multi-mode guided-waves in pipes *Proc. SPIE* **9437** 94371W
- [33] Moustakidis S, Kappatos V, Karlsson P, Selcuk C, Gan T H and Hrissagis K 2014 An intelligent methodology for railways monitoring using ultrasonic guided waves *J. Nondestruct. Eval.* **33** 694–710
- [34] Rizzo P, Bartoli I, Marzani A and di Scalea F L 2005 Defect classification in pipes by neural networks using multiple guided ultrasonic wave features extracted after wavelet processing *J. Press. Vessel Technol.* **127** 294–303
- [35] Comon P 1994 Independent component analysis, a new concept? *Signal Process.* **36** 287–314
- [36] Hyvärinen A and Oja E 2000 Independent component analysis: algorithms and applications *Neural Netw.* **13** 411–30
- [37] Qi A L, Bai H L, Ma H W and Zhang X Y 2012 A method of mechanical defect ultrasonic signal extraction based on ICA *J. Xi'an Univ. Sci. Technol.* **3** 023
- [38] Chen W, Liu T and Wang B 2011 Ultrasonic image classification based on support vector machine with two independent component features *Comput. Math. Appl.* **62** 2696–703
- [39] Liu C, Dobson J and Cawley P 2016 Practical ultrasonic damage monitoring on pipelines using component analysis methods *19th World Conf. Non-Destructive Test*
- [40] Duistermaat J J and Kolk J A 2010 *Distributions* (Boston, MA: Birkhäuser) (<https://doi.org/10.1007/978-0-8176-4675-2>)
- [41] Hyvärinen A and Oja E 2000 A fast fixed-point algorithm for independent component analysis *Int. J. Neural Syst.* **10** 1–8
- [42] Sun B, Yan Z and Wu R 2002 Development of 50AT switch rail *Rail Section Plant of Baotou Steel Union* **28** 19–20
- [43] Hayashi T, Tamayama C and Murase M 2006 Wave structure analysis of guided waves in a bar with an arbitrary cross-section *Ultrasonics* **44** 17–24
- [44] De Marchi L, Marzani A and Miniaci M 2013 A dispersion compensation procedure to extend pulse-echo defects location to irregular waveguides *NDT & E Int.* **54** 115–22